TITLE PAGE

Citation Format: Aleh Sudakou, Heidrun Wabnitz, Lin Yang, Davide Contini, Lorenzo Spinelli,Alessandro Torricelli, Adam Liebert, "Depth selectivity in time-domain fNIRSby analyzing moments and time windows," Proc. SPIE 11639, OpticalTomography and Spectroscopy of Tissue XIV, 116390Q (5 March 2021); doi:10.1117/12.2578518

DOI abstract link:

https://doi.org/10.1117/12.2578518

Depth selectivity in time-domain fNIRS by analyzing moments and time windows

Sudakou, Aleh, Wabnitz, Heidrun, Yang, Lin, Contini, Davide, Spinelli, Lorenzo, et al.

Aleh Sudakou, Heidrun Wabnitz, Lin Yang, Davide Contini, Lorenzo Spinelli, Alessandro Torricelli, Adam Liebert, "Depth selectivity in time-domain fNIRS by analyzing moments and time windows," Proc. SPIE 11639, Optical Tomography and Spectroscopy of Tissue XIV, 116390Q (5 March 2021); doi: 10.1117/12.2578518

SPIE.

Event: SPIE BiOS, 2021, Online Only

Depth selectivity in time-domain fNIRS by analyzing moments and time windows

Aleh Sudakou[1], Heidrun Wabnitz[2], Lin Yang[2], Davide Contini[3], Lorenzo Spinelli[4], Alessandro Torricelli[3,4], Adam Liebert[1]

[1] Nalecz Institute of Biocybernetics and Biomedical Engineering, Trojdena 4, 02-109 Warsaw, Poland
[2] Physikalisch-Technische Bundesanstalt (PTB), Abbestraße 2-12, 10587 Berlin, Germany
[3] Politecnico di Milano, Dipartimento di Fisica, Piazza Leonardo da Vinci 32, 20133 Milan, Italy
[4] Istituto di Fotonica e Nanotecnologie, Consiglio Nazionale delle Ricerche, Piazza Leonardo da Vinci 32, 20133 Milan, Italy

ABSTRACT

Time-domain fNIRS facilitates the elimination of the influence of extracerebral, systemic effects on measured signals since it contains time-of-flight information that is related to the penetration depth. Employing perturbation and Monte-Carlo simulations, we quantitatively characterized and compared the performance of measurands based on moments and time windows of time-of-flight distributions. We extend our analysis to investigate whether higher moments and Mellin-Laplace (ML) moments promise improvements in performance. The comparison is based on spatial sensitivity profiles as well as metrics for relative contrast, contrast-to-noise ratio (CNR), depth selectivity, and the product of CNR and depth selectivity for layered absorption changes. The influence of reduced scattering coefficient, thickness of the superficial layer, and source-detector distance was analyzed. The third central moment performs similarly to variance and is worth considering for data analyzes. Higher order ML moments perform similarly to time windows and they likewise provide variable depth selectivity.

Keywords: Time resolved imaging, light propagation in tissues, fNIRS, perturbation, Monte Carlo, performance assessment, depth selectivity

1. INTRODUCTION

In many of the fNIRS applications, especially in adult humans, it is important and challenging to eliminate the superficial contamination of measured signals, which is typically related to changes in systemic physiological parameters. Time-domain fNIRS is an emerging technology that offers a most promising solution to this issue. By acquiring the distribution of times of flight (DTOF) of photons propagating from source to detector it is possible to achieve depth discrimination of absorption changes. Most of the approaches to analyze measured DTOFs start from a reduced number of quantities characterizing the DTOF profile. Various research groups successfully employed different data types in laboratory and *in-vivo* experiments, in particular, photon counts integrated within various time windows [1], moments [2], or Mellin-Laplace moments [3].

Previously, we introduced depth selectivity as the ratio of sensitivities to deep versus superficial layered absorption changes [4]. A measurand that exhibits higher depth selectivity is more suitable for monitoring absorption changes in the brain. So far, the different data types have been used and investigated separately in numerous studies. Therefore, a comparison of their features on a common basis was lacking until it was addressed by two recent studies of our groups. The first study [5] characterized and compared moments (integral, mean time of flight and variance), photon counts in individual time windows, and ratios of photon counts in different time windows, with respect to depth selectivity as well as robustness against the shape of the instrument response function (IRF). The second study [6] took the contrast-to-noise ratio (CNR) into account and introduced the product of CNR and depth selectivity to rank the overall performance of these measurands, identifying variance as the optimal choice. The present contribution combines aspects of both studies and extends them towards the third central moment, as well as Mellin-Laplace moments, to answer the question whether these are candidates for even better performance than variance.

Optical Tomography and Spectroscopy of Tissue XIV, edited by Sergio Fantini, Paola Taroni, Proc. of SPIE
Vol. 11639, 116390Q · © 2021 SPIE · CCC code: 1605-7422/21/$21 · doi: 10.1117/12.2578518

2. METHODS

2.1 MEASURANDS

The operations to derive the characteristic quantities (or data types, here also referred to as measurands) M under consideration from measured DTOFs $N(t)$ can be represented by:

$$M_G = \int_0^\infty G(t)N(t)dt \,. \tag{1}$$

For time windows, the weight function $G(t)$ is $G \equiv 1$ over time channels (t) within a time window $t_{ak} \le t \le t_{bk}$ and $G \equiv 0$ elsewhere, for the photon count N_k summed up within the k^{th} time window interval. For moments, $G = t^n / N_{\text{tot}}$ for m_n, the normalized moments of order n, and $G = (t - m_1)^n / N_{\text{tot}}$ for m_n^c, the normalized central moments of order n with m_1 being the mean time of flight. The zeroth moment ($n = 0$) is the total photon count N_{tot} ($G \equiv 1$). A detailed discussion of the calculation of moments, time windows, and ratios of time windows was provided in [5].

Mellin-Laplace (ML) transformation leads to generalized moments with a weight function $G = (p^n / n!)t^n e^{-p \cdot t}$ where p is a positive real decay constant [7]. G corresponds to a smooth windowing of the DTOF and the mean time of the n^{th} window is equal to $(n+1)/p$. The width of the window is controlled by p in the exponential term of the product. Smaller values of p imply wider time windows for consecutive values of n. For small values of p (e.g. 0.01 ns^{-1}), the ML transforms approximate the non-normalized, non-central moments m_n of the DTOF, apart from an amplitude factor [7]. We set the value of p to 1 ns^{-1} and the value of n from 0 to 10. The study by Puszka *et al.* [3] presented a method of reconstruction of the optical properties of a turbid medium based on ML transforms and it was shown that using more than 10 orders (n) does not improve the reconstruction result significantly. Importantly, the changes in ML moments as defined here are not independent of the instrumental response function (IRF) [7]. This is not an issue for simulated data but must be considered for measured data. The influence of the parameter p on the ML moments can be addressed in a future study, as well as centralized and normalized ML moments.

Figure 1 illustrates a DTOF $N(t)$, the weight function $G(t)$, and the related integrand $N(t)G(t)$ for the calculation of selected measurands. As expected, $N(t)G(t)$ for the third central moment (m_3^C) extends to longer times compared to lower moments, e.g. variance (V). $N(t)G(t)$ is negative for times less than m_1, which is a consequence of the cubic term. ML moments (for p=1 ns^{-1}) correspond to windowing, as illustrated in Figure 1 (d-f). The higher order ML moments shift towards later times similar to the time windows in Figure 1 (c), and exhibit greater and n-dependent width.

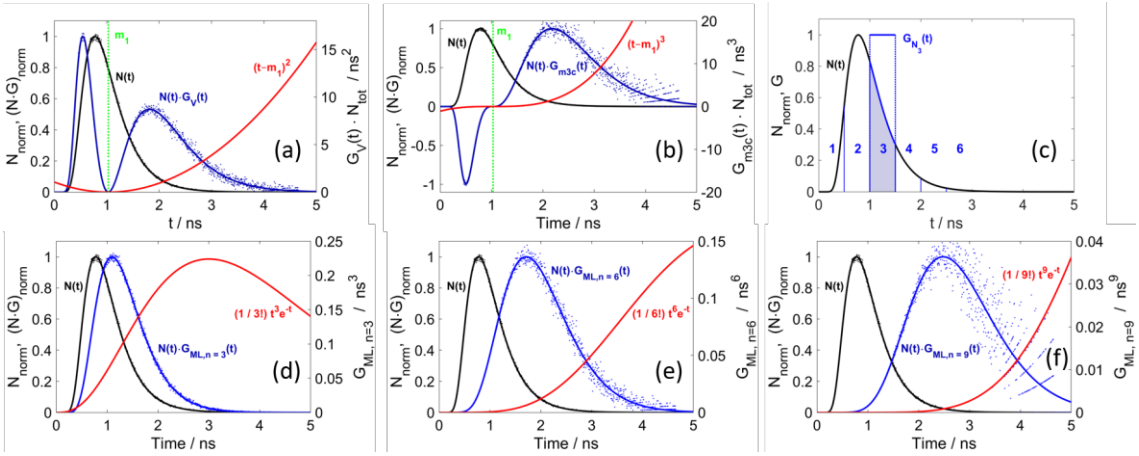

Figure 1. Integrand and its constituents for calculation of variance (a), third central moment (b), six time windows with 500 ps width (c), and the 3$^{\text{rd}}$ (d), 6$^{\text{th}}$ (e), and 9$^{\text{th}}$ (f) ML moments for p = 1 ns^{-1}. $N(t)$ was simulated for a semi-infinite homogeneous medium with reduced scattering coefficient μ_s' = 1 mm^{-1}, absorption coefficient μ_a = 0.01 mm^{-1}, refractive index n = 1.4 and for source-detector separation ρ = 3 cm, based on the diffusion model and extrapolated boundary conditions [8]. $N(t)$ and $G(t)N(t)$ were normalized to their respective maxima. Poisson noise was simulated for $N_{\text{tot}} = 10^6$ and 5 ps width of the histogram time bins.

2.2 PERTURBATION SIMULATIONS

To quantify and compare the sensitivities for the various measurands, we employed a simplified model: a perturbation approach based on the diffusion theory for photon migration and Born approximation for which analytical solutions are available for certain geometries. We assumed a point-like, isotropic source and a point-like detector located at (0, 0, z_0) and at (ρ, 0, 0), respectively, with $z_0 = 1 / \mu_s'$ and ρ being the (fixed) source-detector separation. The z axis is perpendicular to the surface and pointing into the medium. From the perturbed and unperturbed DTOFs, the changes in the various measurands were calculated and hence the 3D sensitivity profiles were obtained by varying the position (x, y, z) of the point-like absorber inside the medium in all three dimensions. A detailed description of the simulations was provided in [5].

2.3 MONTE CARLO SIMULATIONS

DTOFs were generated with Monte Carlo (MC) simulations which used the code introduced by Wojtkiewicz *et al*. [9]. Three MC simulations were carried out: homogeneous medium with μ_a = 0.01 mm^{-1}, 15% increase in absorption in the superficial layer only, and 15% increase in absorption in the deeper layer only. The refractive index was set to 1.33 and the scattering was assumed to be isotropic. The previous study [6] analyzed measurements performed on liquid phantoms and obtained good agreement between measured and simulated data. Simulations were repeated for different values of reduced scattering coefficient (μ_s' = 0.5, 1.0, and 1.5 cm^{-1}), thickness of the superficial layer (d = 5, 10, and 15 mm), and source-detector distance (ρ = 20, 30, and 40 mm). Detailed description of the simulations was provided in [6]. For higher moments, the later photons become more important and hence the integration time limit was extended to 5 ns to encompass more of the DTOF [6].

2.4 PERFORMANCE ASSESSMENT

The performance can be assessed based on objective metrics [6]: relative contrast, CNR, depth selectivity, and product of CNR and depth selectivity. The metrics allow to quantitatively compare the different measurands with respect to sensing small absorption changes in a layered medium. Relative contrast is a percentage change of a measurand (with respect to its baseline value) that results from an increased absorption inside the superficial (first) layer or the deep (second) layer. CNR is the ratio of the change in a measurand and its standard deviation. Depth selectivity can be calculated from perturbation simulations as the ratio of integrated sensitivities in a deep versus a superficial layer. Also, depth selectivity can be calculated from simulated or measured data as the ratio of the contrast in the deep versus superficial layer, given that the small absorption change in both cases is the same. The product of depth selectivity and CNR for the deep layer provides a quantitative measure for ranking the performance of different measurands. Detailed description of the metrics was provided in [6].

The standard deviation of $m_3{}^C$ due to Poisson noise was calculated from the simulated DTOF for the homogeneous case using the following equation, which was obtained from the general formula derived in [10]:

$$\sigma_P^2(m_3^C) = \frac{1}{N_T}\left[9(m_2^C)^3 - 6m_2^C m_4^C - (m_3^C)^2 + m_6^C\right]. \tag{2}$$

The uncertainty of the n^{th} order ML moment can be described by the generic formula:

$$\sigma_{MLT(n,p)} = \sqrt{\sum_i^k \left(\frac{p^n}{n!}\right)^2 t_i^{2n} e^{-2p\cdot t_i} N_i}\ . \tag{3}$$

Apart from counting noise, there are other sources of uncertainty that will not be addressed here. Time-window measurands can be substantially influenced by long tails and afterpeaks of the IRF [5], which can be expected for the considered ML moments as well. Changes in the moments m_1, V and $m_3{}^C$, however, are independent of the IRF if the integration limits encompass the complete DTOF [5]. Moreover, the influences of residual background signal and background noise deserve particular attention, specifically for higher moments.

3. RESULTS AND DISCUSSION

3.1 SENSITIVITY PROFILES

Figure 2 shows several 2D sensitivity profiles, which were obtained by summing the 3D profiles along the *y* direction. The profiles for other measurands can be found in [5] or for ML moments in [3]. The maximum of the sensitivity profile moves deeper as the order of the moment increases and for later time windows. Normalized moments exhibit a superficial region of negative sensitivity, which is quantitatively shown in Figure 3 (a). However, the sensitivity to layered absorption changes is always positive for all measurands considered, which is shown in Figure 3 (b).

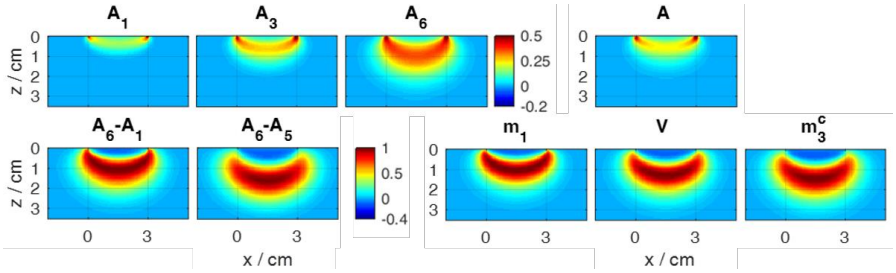

Figure 2. Comparison of sensitivity distributions (integrated over the third dimension and normalized to the maximum in each panel; the relative color bar in each row is valid for all panels in that row) for some of the measurands related to time windows (labelled A_1, A_3, and A_6 for attenuation), ratios of time windows (equivalent to attenuation differences) (A_6–A_1 and A_6–A_5), and statistical moments (A, m_1, V, and m_3^C). The sensitivity distributions for ML moments can be found in [7].

The sensitivity profiles were further analyzed to assess their characteristics. Figure 3 shows depth scans through 3D profiles through the center, as illustrated with the grey lines in the insets. Notably, the ratio between minimum and maximum is very similar for m_1, V and m_3^C. For a layered absorption change, i.e. when $\Delta\mu_a$ occurs in the whole layer at depth z, the sensitivities (S^L) are obtained by integrating over x and y across the whole sensitivity profiles and examples are illustrated in Figure 3 (b) for 2 cm and 3 cm source-detector separations (ρ). The integral (A) has a high sensitivity in the superficial regions, while for higher order moments the sensitivities are situated deeper and the sensitivities to superficial regions are relatively smaller. The dependence on ρ increases with the order of moment. For time windows (shown in [5]), the magnitude of sensitivities grows with time and also the position of the maximum becomes deeper. However, for all time windows the sensitivity to the superficial layer is substantial. On the contrary, for ratios of time windows (shown in [5]), the maxima are deeper and the sensitivities to the superficial layer are much lower.

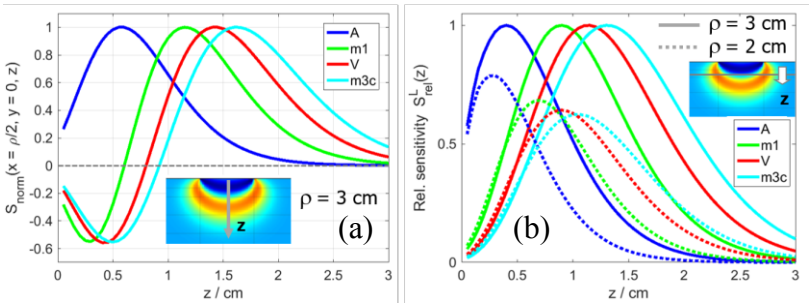

Figure 3. Depth-dependent sensitivities for moments. (a) Sensitivities to a point-like absorption change at depth z in the center between source and detector, normalized to their maxima. (b) Comparison of sensitivities to absorption changes in an infinitesimally thin layer at position z for ρ = 2 cm (dashed lines) and 3 cm (solid lines). Sensitivities for each moment were normalized to their maxima for ρ = 3 cm. The insets schematically show the z scans in relation to the 3D sensitivity profiles.

Some quantitative characteristics of the depth-dependent sensitivities for the moments and time-window measurands are shown in Figure 4. The position of the maxima increases for higher moments. The full width at half maximum (FWHM) shows the span between the 50% points where the sensitivity at the smaller z drops below 50% of the maximum. The FWHM can be regarded as a measure of depth resolution. For the cases considered here, it always remains larger than 1 cm.

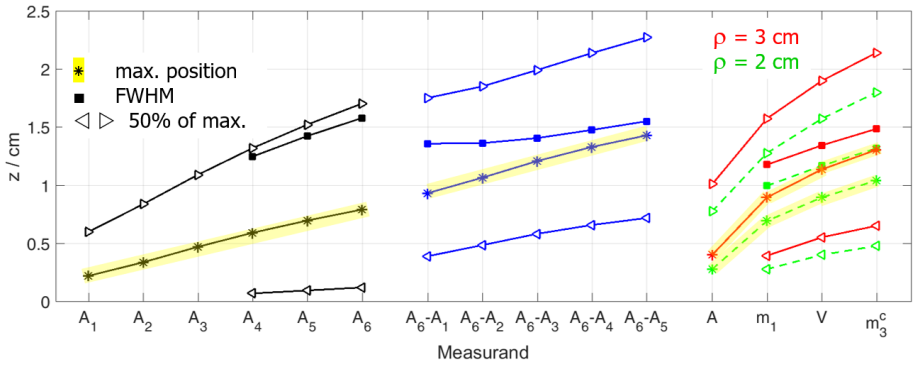

Figure 4. Characteristics of the z-dependent sensitivities to layered absorption changes for all measurands, comparing the positions of their maxima (*), the FWHM (■), and z positions at 50% of maximum sensitivity toward smaller (◁) and larger (▷) z values. Parameters for time-window measurands (attenuation A_k in 6 consecutive time windows of 500 ps width and their differences) were calculated for $\rho = 3$ cm and the values are valid for 2 cm as well. Results for moments are plotted for $\rho = 2$ cm (green dashed lines) and $\rho = 3$ cm (red solid lines).

3.2 OBJECTIVE METRICS

A more complete assessment of measurands' performance requires the consideration of noise, which was done by calculating the *CNR* using the Poisson statistics to model the major source of noise in photon counting measurements. The quantitative analyses for all measurands, and in particular for m_3^C and ML moments, are presented in Figure 5 for relative contrast, both for the superficial and deep layer (first row), *CNR* for the deeper layer (CNR_2) (second row), depth selectivity (third row), and the product of CNR_2 and depth selectivity (fourth row). The analysis was repeated for different μ_s' (first column), thickness of the first layer (second column), and ρ (third column). The results for all possible ratios of late and early time windows were presented in [6] as well as a discussion of the dependence on μ_s', thickness of the first layer, and ρ.

m_3^C shows an improvement in the relative contrast and depth selectivity, but a smaller CNR_2 compared to lower moments. The product of CNR_2 and depth selectivity is similar for V and m_3^C under all considered parameter variations, suggesting that m_3^C is worth considering for the analysis.

ML moments behave similarly to time windows, where the higher order ML moments correspond to later time windows. This is particularly seen when comparing the relative contrasts for the superficial and deep layer as well as the resulting depth selectivity. However, the relative contrasts for time windows are independent of ρ, in agreement with [11], unlike for ML moments. The dependence of depth selectivity on ρ decreases for higher order ML moments, such that higher order ML moments behave more similar to time windows with respect to ρ dependence as well. ML moments show lower depth selectivity, but higher CNR_2, in comparison to time windows. The product of depth selectivity and CNR_2 is similar to that of time windows, staying below the product for m_1, V and m_3^C.

A more informative way to analyze the product of CNR_2 and depth selectivity (fourth row in Figure 5) is to plot CNR_2 versus depth selectivity, which is shown in Figure 6 for different values of ρ. The total number of photons depends on ρ, corresponding to a detection system with fixed sensitivity. The data points for m_3^C almost overlap those for V, but for different values of ρ. In particular, CNR_2 and depth selectivity of m_3^C at $\rho = 15$ and 20 mm are almost equal to the values for V at $\rho = 20$ and 25 mm, respectively. This agrees with the sensitivities of V and m_3^C shown in Figures 2 and 3, and with the general knowledge of how sensitivities for moments depend on ρ (Figure 3(b)). Depth selectivity, as well as noise, increase for higher moments and for longer ρ. The calculation of m_3^C depends strongly on the late photons and more so for longer ρ (as seen in Figure 1 (b)) and the simulated DTOFs were limited to 5 ns, which causes errors for m_3^C for ρ more than 40 mm. ML moments for the lowest orders (e.g. $n = 0$ and $n = 3$) show a dependence on ρ that resembles the results for moments. On the contrary, ML moments for the higher orders (e.g. $n = 9$) resemble the results for time windows.

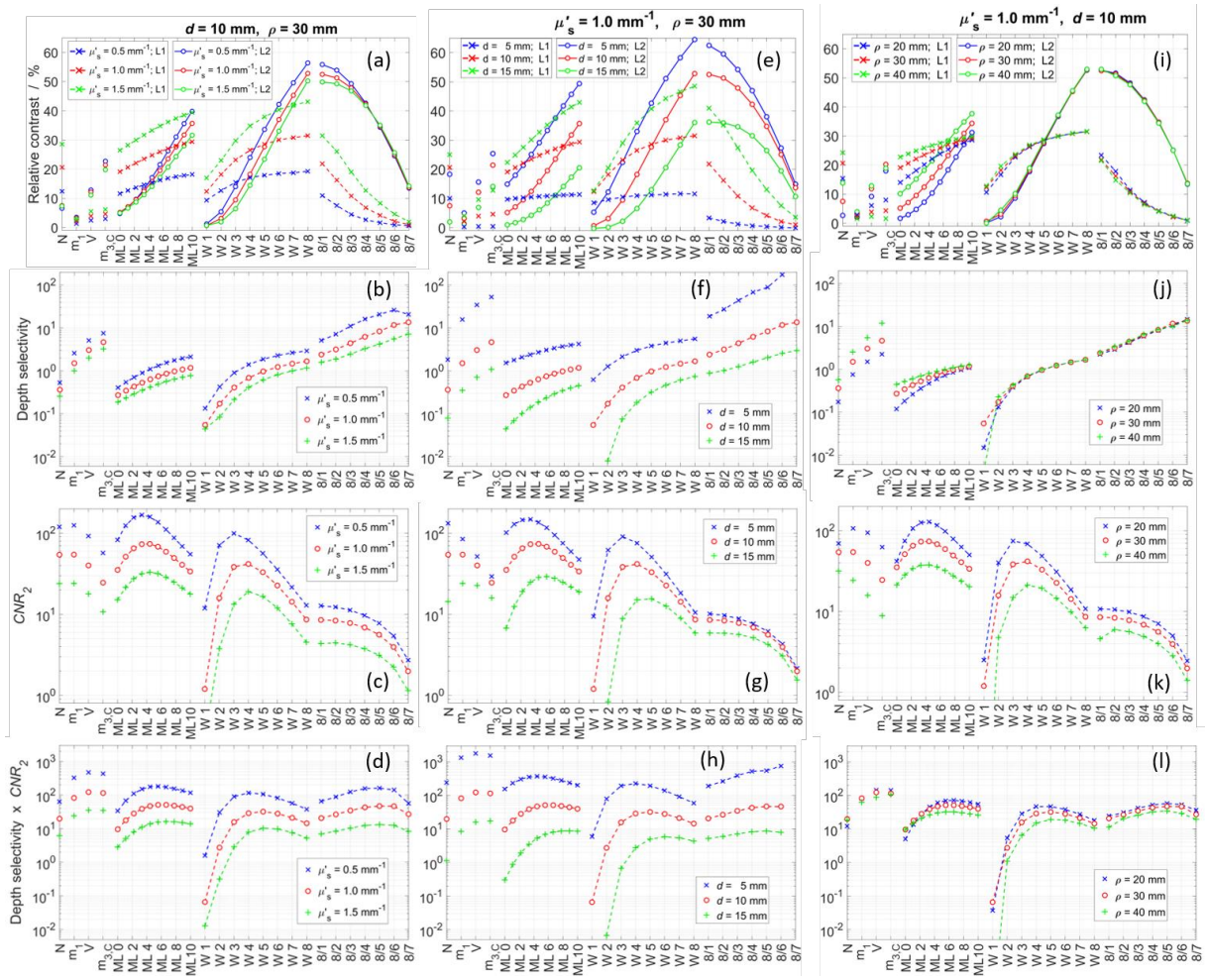

Figure 5. Quantitative comparison of measurands using relative contrast (first row), contrast-to-noise ratio (CNR_2) (second row), depth selectivity (third row) and product of CNR_2 and depth selectivity (fourth row), repeated for different parameters of the model: (a-d) reduced scattering coefficient (μ_s'), (e-h) thickness of superficial layer (d), and (i-l) source-detector separation (ρ). Notations L1 and L2 in (a, e, i) correspond to contrast in superficial and deep layers, respectively.

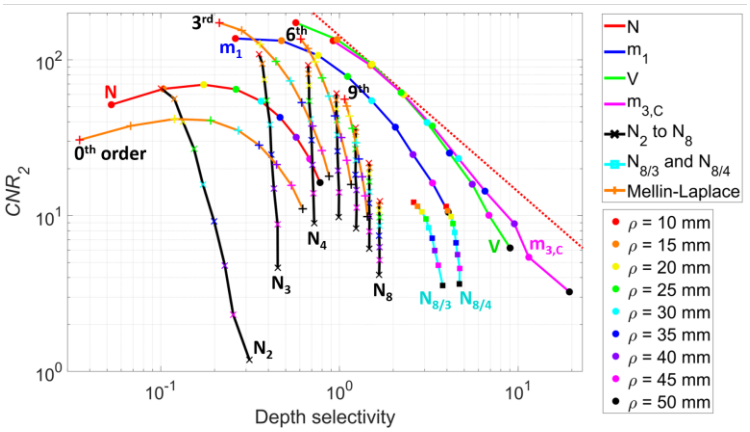

Figure 6. CNR_2 vs. depth selectivity for different measurands for various source-detector distances ρ, from 10 to 50 mm, and color-coded according to legend. The ML moments shown are 0th, 3rd, 6th, and 9th order. Total number of photons N_{tot} changes with ρ corresponding to a measurement with a fixed detection sensitivity. The red line shows the constant value of the highest product of CNR_2 and depth selectivity, which was attained for m_3^C at 15 mm and V at 20 mm.

4. CONCLUSIONS

The previous studies [2, 3] introduced a method to quantitatively compare different measurands regarding their suitability for selectively detecting absorption changes in the brain, using phantom measurements or simulated data. This method relies on the metrics: depth selectivity and contrast-to-noise ratio (CNR). Since both are important, their product served as ranking criterion. The current study applied the same methods for m_3^C and specific ML moments with varying order n and fixed exponential factor p in addition to the previously considered measurands N, m_1, V, time windows, and ratios of time windows. The analyses of these metrics in combination with the underlying spatial sensitivity distributions illustrate the features of the different measurands, which are crucial for the optimization and comparability of the various analysis procedures in time-domain fNIRS.

A major finding of the present study is the fact that m_3^C performs similarly well as V and is worth considering for data analyzes. Results obtained for m_4^C (not shown here) indicate that the product of depth selectivity and CNR is smaller for higher central moments compared to m_3^C. ML moments with varying order n provide variable depth selectivity and the ranking results show some similarities to statistical moments or time windows depending on the ML moment's order.

It would be interesting to subject other measurands to the same method of performance evaluation. Here, normalized as well as central ML moments are other candidates that also may potentially combine the flexibility of time windows with the robustness of (central) moments against the IRF. Another point of interest in the context of depth-resolved reconstruction of absorption changes is the search for measurands with enhanced selectivity for superficial tissue very close to the surface. Tuning the exponential factor p in such ML moments could be beneficial in this respect.

5. ACKNOWLEDGEMENTS

This project has received funding from the European Union's Horizon 2020 Marie Skłodowska-Curie Innovative Training Networks (ITN-ETN) programme, under grant agreement no 675332, BitMap, and from The National Science Centre (NCN), Poland, under grant agreement no (UMO-2019/33/N/ST7/02918, UMO-2014/15/B/ST7/05276).

6. REFERENCES

1. J. Selb, J. J. Stott, M. A. Franceschini, A. G. Sorensen, and D. A. Boas, "Improved sensitivity to cerebral hemodynamics during brain activation with a time-gated optical system: analytical model and experimental validation," J. Biomed. Opt. 10(1), 011013 (2005).
2. A. Liebert, H. Wabnitz, J. Steinbrink, H. Obrig, M. Möller, R. Macdonald, A. Villringer, and H. Rinneberg, "Time-resolved multidistance near-infrared spectroscopy of the adult head: Intracerebral and extracerebral absorption changes from moments of distribution of times of flight of photons," Appl. Opt. 43 (15), 3037–3047 (2004).
3. A. Puszka, L. Hervé, A. Planat-Chrétien, A. Koenig, J. Derouard, and J.-M. Dinten, "Time-domain reflectance diffuse optical tomography with Mellin-Laplace transform for experimental detection and depth localization of a single absorbing inclusion," Biomed. Opt. Express. **4**, no. 4, 569–83 (2013).
4. H. Wabnitz, A. Jelzow, M. Mazurenka et al., "Performance assessment of time-domain optical brain imagers, part 2: nEUROPt protocol," J. Biomed. Opt. **19**, 086012 (2014).
5. H. Wabnitz, D. Contini, L. Spinelli, A. Torricelli, and A. Liebert, "Depth-selective data analysis for time-domain fNIRS: moments vs. time windows," Biomed. Opt. Express **11**, 4224–4243 (2020).
6. A. Sudakou, L. Yang, H. Wabnitz, S. Wojtkiewicz, and A. Liebert, "Performance of measurands in time-domain optical brain imaging: depth selectivity versus contrast-to-noise ratio," Biomed. Opt. Express **11**, 4348-4365 (2020).
7. L. Hervé, A. Puszka, A. Planat-Chrétien, and J.-M. Dinten, "Time-domain diffuse optical tomography processing by using the Mellin–Laplace transform," Appl. Opt. **51**, 5978 (2012).
8. D. Contini, F. Martelli, and G. Zaccanti, "Photon migration through a turbid slab described by a model based on diffusion approximation I Theory," Appl. Opt. **36**, 4587-4599 (1997).
9. S. Wojtkiewicz, and A. Liebert, "Parallel, multipurpose Monte Carlo code for simulation of light propagation in segmented tissues," Biocybernetics and Biomedical Engineering (in press 2021).
10. A. Jelzow, "In vivo quantification of absorption changes in the human brain by time-domain diffuse near-infrared spectroscopy," PhD Thesis, TU Berlin (2013).
11. S. Del Bianco, F. Martelli, and G. Zaccanti, "Penetration depth of light re-emitted by a diffusive medium: Theoretical and experimental investigation," Phys. Med. Biol. 47(23), 4131-4144 (2002).